Analysis of a passive microforce sensor based on magnetic spings and upthrust buoyancy.

Ali Cherry, Joël Abadie, Emmanuel Piat

Analysis of a passive microforce sensor based on magnetic springs and upthrust buoyancy

A. Cherry, J. Abadie and E. Piat

Femto-st Institute - UMR CNRS 6174, UFC, ENSMM, UTBM, France

Abstract

This paper is focused on the design and modeling of a new micro and nano force sensor using magnetic springs. The force sensitive part is a macroscopic horizontal rigid platform used as a floating seismic mass. This platform presents a naturally stable equilibrium state for its six degrees of freedom (dof) thanks to the combination of upthrust buoyancy and magnetic forces. This force sensor allows the measurement of the external horizontal force and the vertical torque applied to the platform. Thanks to the magnetic springs configuration used, the seismic mass presents a 0.02 N/m horizontal mechanical stiffness (similar to the stiffness of a thin AFM micro-cantilever). The measurement range typically varies between ± 50 μN. The resolution depends on the displacement sensors used to measure the seismic mass displacement and on the environmental conditions (ground, liquid and air vibrations). In steady state, this displacement is proportional to the applied force. Resolution of less than 10 nN can be reached with the use of an anti-vibration table.

Key words: micro and nano force sensor, passive measurement, sensor calibration, magnetic spring, upthrust buoyancy.

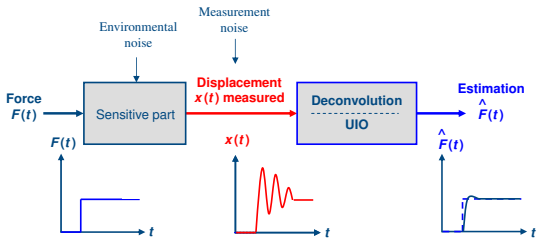

Fig. 1. Passive force estimation.

1. Introduction

The nano and micro force measurement field is an emergent market with a large potential growth. Are concerned by this market nanomaterial companies, micromechanical and micro engineering business, the numerous firms using micro encapsulation, research laboratories in the field of micro and nano advanced technologies and finally the more restricted market of biomedical research which needs to characterize responses of living cells to mechanical stimuli.

Micro and nano force sensors design is constrained by the fact that only force effects can be directly measured.

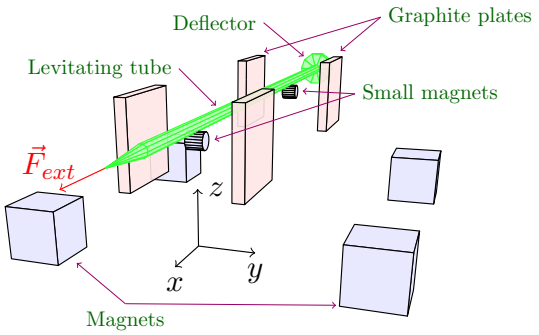

Fig. 2. Nanoforce sensor based on passive diamagnetic levitation. The graphite plates produce repulsive forces that stabilize the glass tube along y direction.

Because of this, a force sensitive part is needed to observe these effects. This sensitive part acts as a transducer that converts the applied force F into a displacement (see figure 1). This displacement is measured with an appropriate displacement sensor. To estimate the input force F, it is necessary to do a deconvolution or to use an Unknown Input Observer (UIO) that calculates an estimation $\hat{F}$ of that force. Most of the transducers that have a large bandwidth are associated with a very simple deconvolution law because designers assume that the force estimation $\hat{F}$ is proportional to the measured displacement.

Email address: jabadie@femto-st.fr (A. Cherry, J. Abadie and E. Piat).

Because force effects can be measured in many different ways, micro and nano force sensor designs are numerous. The majority is based on monolithic elastic microstructures which are generally microcantilevers [1] coupled or not with mechanical deformation amplifier: AFM based microforce sensors using two or four quadrants photodectectors [2] or interferometry principle [3], piezoresistive microforce sensors which use the variation of the piezoresistive layer resistance when a force is applied [4], capacitive microforce sensors which make use of changes in capacitance between two metal plates when their distance change during force application [5], piezoelectric microforce sensors which generate a voltage when they are stressed by a force [6], etc. Because maximum deformations of monolithic microstructures are usually low, these sensors are mostly limited in range of force measurement but have a large bandwidth. A few sensors can exhibit larger deformations or displacements. For instance, the maximum deformation of the nanoforce sensor presented in [7] is several dozen micrometers thanks to a special compliant mechanical design with a very low stiffness. Another sensor using a seismic mass, and which greatly inspired the theorical study presented here, is based on passive diamagnetic levitation [8]. The seismic mass is a ten centimeters long levitating glass capillary tube (like a micropipet) on which two small magnets (less than 1 mm^3) are stuck (see figure 2). To levitate passively, the capillary tube mass must be less than 100 milligrams. This levitating part is used as a one direction force sensing device (along its longitudinal axis $\boldsymbol{x}$). This sensor is characterized by a second order linear force-displacement dynamic (badly damped) which remains linear on very long displacements ($\pm$1.5 mm) and thus can measure a wide range of microforces. The longitudinal displacement x of the levitating part is measured with a confocal chromatic sensor on the rear deflector (see figure 2). This displacement is proportional to the force $\boldsymbol{F}_x^{ext}$ applied when steady-state is reached. The stiffness is adjustable with typical value equal to 0.01 $N.m^{-1}$ and a bandwidth of a few hertz. The resolution depends on the seismic mass displacement resolution and on noises induced by environmental conditions (ground and air vibrations). Resolution of 1 nN is easily reached with an anti-vibration table and a CL2 confocal chromatic sensor (distributed by STIL SA).

This paper deals with the design and the modeling of a new micro and nano force sensor mostly inspired by the micro and nano force sensor using diamagnetic levitation previously described. The new sensor is based on the same magnetic spring principle. The main difference is the replacement of diamagnetic effects by upthrust buoyancy. The role of the magnetic spring and the upthrust buoyancy is first presented and explained on a simplified mechanism, the Magnetic Spring Floating Mechanism (MSFM). Then the MSFM is modeled in order to analyze the stability in the different directions. Because one MSFM is not optimized for force sensing, a sensitive platform including two MSFM is presented. The platform is parameterized, modeled and optimized for measuring the two components of an horizontal input force and a vertical input torque. The design is ended by the modeling and the optimization of the configuration of the sensors used to measure the displacement of the sensitive platform. A linear model is presented and compared to the physical model of the optimized platform. The linear model is used to define the important parameters of the sensor. The experimental setup is then presented. The calibration process is performed on the experimental setup in order to determine the parameters of the sensor. These parameters are then used to calculate an estimation of the input force and torque. Finally the sensor is experimentally tested and two potential applications are given.

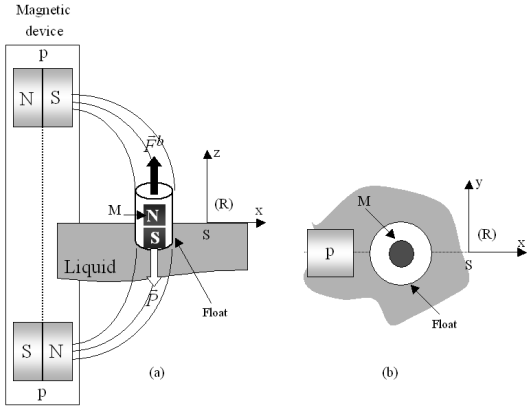

Fig. 3. (a) Side view: buoyancy tank (b) Top view.

2. The Magnetic Spring Floating Mechanism

The force sensor presented in this paper is based on the use of magnetic springs and upthrust buoyancy. Repulsive upthrust buoyancy, instead of repulsive diamagnetic effects, offers the possibility to support heavier seismic mass if necessary. It also allows an easy exploitation of three degrees of freedom (dof) in the liquid surface plane. The Magnetic Spring Floating Mechanism (MSFM) is the starting point for the design of our sensor. This MSFM is composed of a permanent magnet M fixed in a float (see figure 3). M floats at the surface of a liquid. It is under the influence of two fixed magnets p placed below and above the liquid surface. Magnets p (5×5 mm) are placed such that their north and south poles are in opposite directions. The distance between the two magnets p influences the value of magnetic forces applied on the floating magnet M. The magnets p and M are made of NdFeB and the floating magnet M has a radius of 2 mm and a height of 2.5 mm. With such a configuration, the floating part is stable in the plan (xOy) (see section 2.5) thanks to the magnetic forces generated by the magnetic device [9]. The upthrust buoyancy acting against the gravity provides a stability along $\boldsymbol{z}$ axis in the reference frame R shown in figure 3 (see section 2.4). The upthrust buoyancy has no action in the plan (xOy). Both upthrust buoyancy and magnetic forces provide stability around $\boldsymbol{x}$,

$\boldsymbol{y}$ and $\boldsymbol{z}$.

2.1. *Static modeling of the MSFM*

In this section, only the principle of force measurement according to $\boldsymbol{x}$ direction is presented. The center of gravity G_f of the floating magnet M is supposed belonging to the plan (xOy). At the equilibrium state position, four external forces described below are applied on the floating magnet M.
The top magnet p applies an attractive force, called $\boldsymbol{F}^{att}$, on M. The bottom magnet p applies also an attractive force called $\boldsymbol{F}'^{att}$ on M obtained symmetrically to the plan (xOy). We note $\boldsymbol{F}^{mag}$ the vectorial sum of $\boldsymbol{F}^{att}$ and $\boldsymbol{F}'^{att}$. The third force is the upthrust buoyancy called $\boldsymbol{F}^{b}$ applied by the liquid along $\boldsymbol{z}$ at the center of gravity of the float which is supposed to be superimposed to G_f. The fourth force $\boldsymbol{P}$, also acting along $\boldsymbol{z}$, is the total weight of the float. When an unknown external force $\boldsymbol{F}^{ext}$ is applied at the center of gravity G_f of M, the new stable equilibrium state is obtained applying the principle of static at the float center of gravity $G_f(x_{G_f}, y_{G_f}, z_{G_f})$:

$$\boldsymbol{F}^{mag} + \boldsymbol{F}^{ext} + \boldsymbol{P} + \boldsymbol{F}^{b} = \boldsymbol{0} \tag{1}$$

with:

$$\boldsymbol{F}^{mag} = \boldsymbol{F}^{att} + \boldsymbol{F}'^{att} \quad \texttt{and} \quad \boldsymbol{F}^{b} + \boldsymbol{P} = 0 \tag{2}$$

The external force $\boldsymbol{F}^{ext}$ is now assumed to be applied only in the plan (xOy). The components along $\boldsymbol{z}$ of $\boldsymbol{F}^{att}$ and $\boldsymbol{F}'^{att}$ cancel each other. Equation (1) projected in the plan (xOy) gives the vectorial equation:

$$\boldsymbol{F}^{ext} = -\boldsymbol{F}^{mag}.$$

Under the previous assumption, the determination of the external force $\boldsymbol{F}^{ext}$ in the plan (xOy) is conditioned by the determination of the magnetic force $\boldsymbol{F}^{mag}$ applied on G_f.

2.2. *Evaluation of* $\boldsymbol{F}^{mag}$

The magnetic field produced at a point T by a permanent magnet modeled by a surface distribution of loads is given by [10]:

$$\begin{aligned}\boldsymbol{B}^{mag}(T) = &\iint_{S^+} \frac{J}{4\pi}\frac{\boldsymbol{AT}}{|\boldsymbol{AT}|}dS^+ \\ &+ \iint_{S^-} \frac{-J}{4\pi}\frac{\boldsymbol{BT}}{|\boldsymbol{BT}|}dS^-\end{aligned} \tag{3}$$

where A and B are two points belonging to the two charged surfaces of the magnet S^+ and S^-.

The determination of the field components $B_x(T)$, $B_y(T)$ and $B_z(T)$ at the point T can be done by the calculation of the equation (3) along $\boldsymbol{x}$, $\boldsymbol{y}$ and $\boldsymbol{z}$. The magnetic force applied on the magnet M is given by [8]:

$$\boldsymbol{F}^{mag} = \int_V \boldsymbol{\nabla}\boldsymbol{B}^{mag}(T)\cdot\boldsymbol{m}_M \cdot dv \tag{4}$$

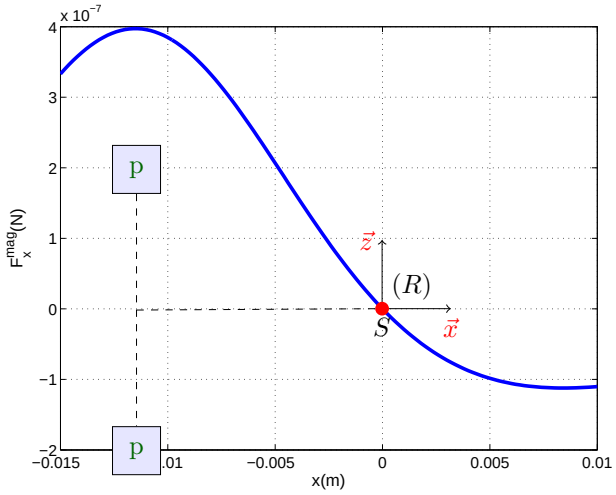

Fig. 4. Magnetic force along $\boldsymbol{x}$ produced by the 2 permanent magnets p when $z = 0$ and $y = 0$.

where $\boldsymbol{B}^{mag}(T)$ is the field produced by both magnets p at a point T inside the magnet M. V is the volume of the magnet M and $\boldsymbol{m}_M$ its magnetization. This magnetization is $8.89 \times 10^4\ A \cdot m^{-1}$ in this study.

Figure 4 presents the evaluation of the magnetic force F_x^{mag} along $\boldsymbol{x}$ when $z = 0$ and $y = 0$. In this configuration, F_y^{mag} and F_z^{mag} are null. The derivative of this curve gives the magnetic stiffness $K_m^x = dF_x/dx$ along $\boldsymbol{x}$. On this curve, the point S corresponds to the equilibrium point of the float when F_x^{ext} is null. S is the origin of reference frame R. In our design $\|LS\|$=11.7 mm with L the center of upper and lower magnets p. In case of small displacements around S, F_x^{mag} is assumed linear in displacement:

$$F_x^{mag} = K_m^x \cdot x \tag{5}$$

Thus, the determination of F_x^{mag} is possible with only the knowledge of the floating magnet position x. This stiffness depends on the distance between the top and the bottom magnets p and on the magnetic characterizations of magnets p and M.

2.3. *Dynamic study of the MSFM*

The dynamic equilibrium along $\boldsymbol{x}$ is given by the following equation:

$$F_x^{ext} + F_x^{mag} + F_x^{f} + F_x^{p} = m\ddot{x} \tag{6}$$

in which F_x^{ext} is the external force applied on the floating magnet M along $\boldsymbol{x}$. F_x^{mag} is given by equation (5) in case of small displacements around S. F_x^f is the viscous friction force between the float and the liquid (atmosphere influence is neglected). Like for the magnetic force, in case of small velocities it is possible to write:

$$F_x^f = K_f^x \cdot \dot{x} \tag{7}$$

in which K_f^x is the viscous damping coefficient. Finally, F_x^p is the total perturbation force, like capillary force (which

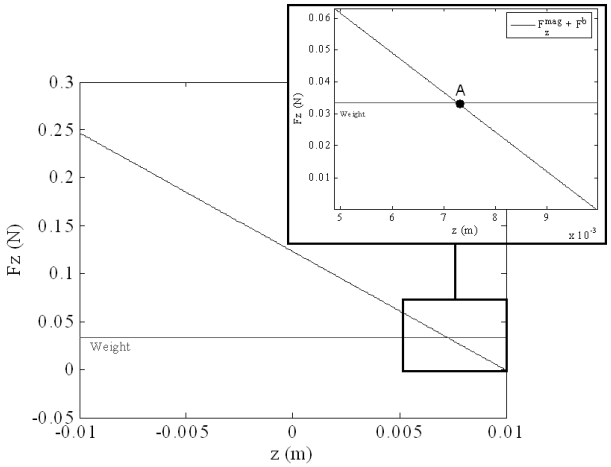

Fig. 5. Evolution of the total force according to $\boldsymbol{z}$

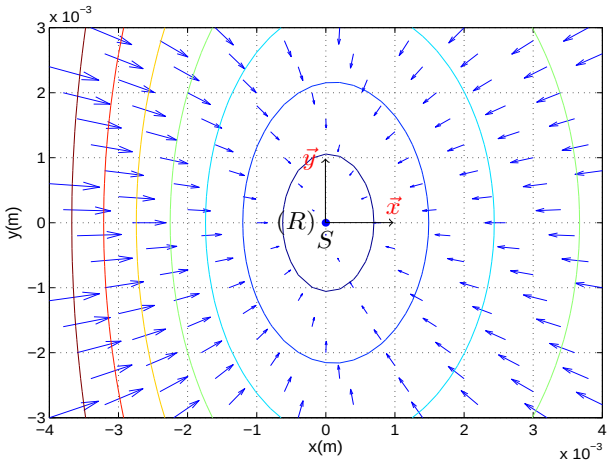

Fig. 6. Field of magnetic forces in the plan (xOy).

disappears in case of symmetric meniscus) and like the delayed return wave of water generated by the displacement of the float and reflected on the edges of the container. According to the reference frame R, the equation (6) becomes finally:

$$F_x^{ext} + F_x^p = m\ddot{x} + K_f^x \dot{x} + K_m^x x \tag{8}$$

2.4. *Stability of the float along* $\boldsymbol{z}$

Passive levitation is commonly unstable. This result was shown theoretically for electrostatic case by Earnshaw in 1842 [11] and for both electrostatic and magnetic cases by Braunbek [12]. Because of this, a small permanent magnet M in levitation between two fixed cubic magnets p cannot be in a stable equilibrium. A slight upward displacement of M results in a greater attraction of the magnetic force $\boldsymbol{F}^{att}$ and M continues to rise until it reaches the upper magnet. Any slight downward displacement of M results in a greater attraction magnetic force $\boldsymbol{F}'^{att}$ and M continues to fall until it reaches the lower magnet.

Like in diamagnetic levitation, it is possible to passively stabilize the unstable equilibrium state of M with an additive repulsive force. Repulsive upthrust buoyancy can be used instead of diamagnetic effects when the sensitive part mass becomes greater than several hundred of milligrams. Figure 5 shows the evolution of the sum of the forces applied on the floating part along $\boldsymbol{z}$ excepted the weight. These forces are the magnetic forces $(F_z^{att} + F_z'^{att})$ applied by top and bottom magnets p on M and the upthrust buoyancy $\boldsymbol{F}^b$ applied by the water on the float. The zoomed-figure (on the right) shows the evolution between 7.5 mm and 10 mm. We note a specific position A where $F^b = mg$. At this point, the weight is completely compensated by the total external force applied on the floating part. A slight upward displacement of M results in a external force lower than the weight (see figure 5) and thus the floating part comes back to A. Any slight downward displacement of M results in an external force higher than the weight and thus the floating part also comes back to A. Thus, the point A is a stable equilibrium point according to $\boldsymbol{z}$.

2.5. *Stability of the float in the plan* (xOy)

Figure 6 shows the field of magnetic force $\boldsymbol{F}^{mag}$, in the plane (xOy), applied by the magnets p on the float. The point S is the stable equilibrium position of the magnet M. At this point, the magnetic force generated by p is null. This stability in the horizontal plan makes possible to extend the floating-magnetic principle described in section 2.1 to measure the components $(\boldsymbol{F}_x^{ext}, \boldsymbol{F}_y^{ext}, \zeta^{ext})$ of an external force. The new external force sensitive element is a floating platform. The platform mass is suspended against gravity by the combined upthrust buoyancy of floats placed at its corners.

3. Seismic platform analysis

Practically, a horizontal force applied on the edge of the float will produce an unexpected rotation of the float. This rotation makes the MSFM unuseable for microforce sensing. No significant magnetic torque holds the float to a defined rotation angle. To avoid this rotation, a design including two MSFM associated with a bigger float is studied.

3.1. *Optimization of the platform configuration*

Figure 7 represents a parameterized configuration of one MSFM. The float is replaced by a platform. Magnet M is placed at a corner. There is only one couple of magnets p oriented with an angle α and generating a force $\boldsymbol{F}^{mag}$ on the magnet M. The shape of the platform is undefined at this step.

Let R_1 be the reference frame of $(S,\boldsymbol{x}_1,\boldsymbol{y}_1)$ with S the stable equilibrium position of M. The platform is moving freely according to a fixed reference frame $R_0(O, \boldsymbol{x}_0, \boldsymbol{y}_0)$.

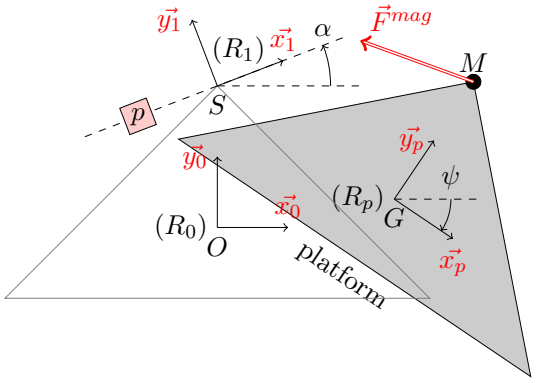

Fig. 7. Platform with a parametrized MSFM (top view)

Let $R_p(G, \boldsymbol{x}_p, \boldsymbol{y}_p)$ be a reference frame related to the platform with :

$$G = \begin{bmatrix} X \\ Y \end{bmatrix}_{/R_0} \quad and \ (\boldsymbol{x}_0, \boldsymbol{x}_p) = \psi$$

X and Y are the coordinates of G in the reference frame R_0. When the platform is on its initial position, both reference frames R_0 and R_p are superimposed. M and S are also superimposed in this case.

3.2. *Change of reference frame*

The reference frame change for a point M belonging to the platform, in the general case, is done by the following transformation:

$$M_{/R_1} = P_{10}[(P_{0p} \cdot M_{/R_p}) + G_{/R_0} - S_{/R_0}] \qquad (9)$$

P_{01} and P_{0p} are the crossing matrices from R_1 to R_0 and from R_p to R_0:

$$P_{10} = [P_{01}]^{-1} = \begin{bmatrix} cos\alpha & sin\alpha \\ -sin\alpha & cos\alpha \end{bmatrix}, \ P_{0p} = \begin{bmatrix} cos\psi & sin\psi \\ -sin\psi & cos\psi \end{bmatrix}$$

where α is the angle formed by the two reference axes $\boldsymbol{x}_1$ and $\boldsymbol{x}_0$ and ψ is the angle formed by the two reference axes $\boldsymbol{x}_p$ and $\boldsymbol{x}_0$.

The reference frame change for the magnetic force $\boldsymbol{F}^{mag}$, under the same conditions, is done by the following transformation:

$$\boldsymbol{F}^{mag}_{/R_0} = P_{01} \cdot \boldsymbol{F}^{mag}_{/R_1} \qquad (10)$$

3.3. *Analytical expression of* $\boldsymbol{F}^{mag}$

The knowledge of analytical expression of the magnetic force $\boldsymbol{F}^{mag}$ is necessary to build the future dynamic model of the platform. This calculation is done in reference frame R_0. Figure 6 shows that iso-forces are elliptic in the immediate proximity of point S. This allows to write :

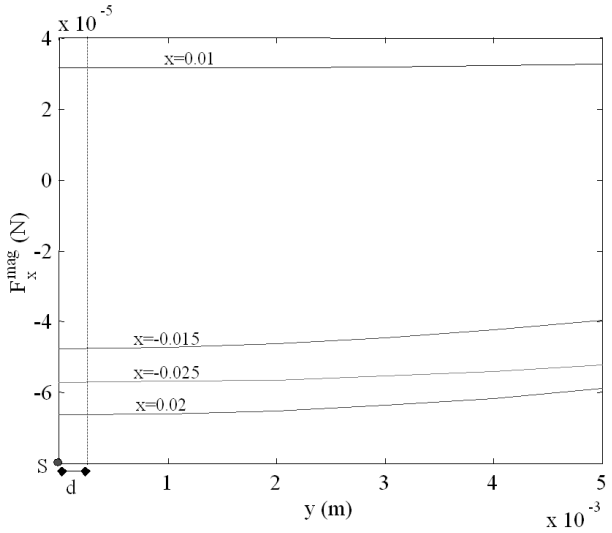

Fig. 8. Magnetic force F_x^{mag} along $\boldsymbol{y}$ and for different values of x.

$$\boldsymbol{F}^{mag}_{/R_1} = \begin{bmatrix} F_x^{mag} \\ F_y^{mag} \end{bmatrix}_{/R_1} = \begin{bmatrix} K_m^x & 0 \\ 0 & K_m^y \end{bmatrix} \begin{bmatrix} x \\ y \end{bmatrix}_{/R_1} \qquad (11)$$

with K_m^x and K_m^y the magnetic stiffness along $\boldsymbol{x}$ and $\boldsymbol{y}$.

The more M is faraway from S, the less equation (11) is correct. Figure 8 shows the component F_x^{mag} along $\boldsymbol{y}$ for different values of x. If the model (11) was always correct, F_x^{mag} should be independent of y, which is not the case on the figure. Nevertheless, smaller is the external force, smaller is the displacement d in figure 8 and better is the model (11). Thus, the relative error induced by this model (compared to the external force) is coherent with the external force to be measured.

According to equations (9), (10) and (11):

$$\boldsymbol{F}^{mag}_{/R_0} = P_{01} \cdot K_m \cdot P_{10}[(P_{0p} \cdot M_{/R_p}) + G_{/R_0} - S_{/R_0}] \qquad (12)$$

thus:

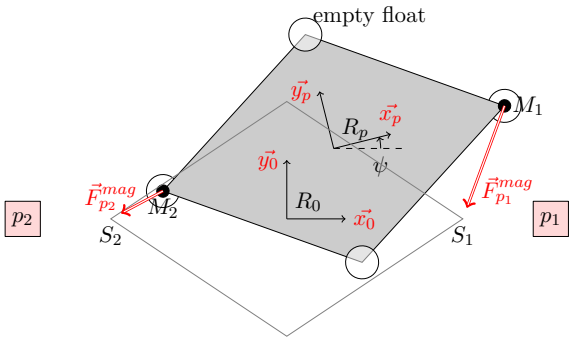

Fig. 9. Final magnetic configuration of the platform (top view)

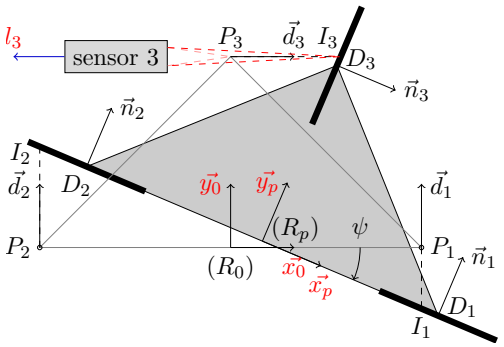

Fig. 10. Optimized placement and configuration of the confocal sensors (sensors 1 and 2 are not shown)

$$F_x^{mag}/_{R_0} = (sin\alpha \cdot K_m^x \cdot cos\alpha \cdot x_M + sin^2\alpha \cdot K_m^y \cdot y_M - cos^2\alpha \cdot K_m^x \cdot y_M + cos\alpha \cdot K_m^y \cdot sin\alpha \cdot x_M)sin\psi + (-sin^2\alpha \cdot K_m^y \cdot x_M + cos^2\alpha \cdot K_m^x \cdot x_M + cos\alpha \cdot K_m^x \cdot sin\alpha \cdot y_M + sin\alpha \cdot K_m^y \cdot cos\alpha \cdot y_M)cos\psi + (sin\alpha \cdot K_m^x \cdot cos\alpha + cos\alpha \cdot K_m^y \cdot sin\alpha)y + (-sin^2\alpha \cdot K_m^y + cos^2\alpha \cdot K_m^x)x + sin^2\alpha \cdot K_m^y \cdot x_M - sin\alpha \cdot K_m^y \cdot cos\alpha \cdot y_M - cos^2\alpha \cdot K_m^x \cdot x_M - cos\alpha \cdot K_m^x \cdot sin\alpha \cdot y_M$$

$$F_y^{mag}/_{R_0} = (-sin^2\alpha \cdot K_m^x \cdot x_M + sin\alpha \cdot K_m^y \cdot cos\alpha \cdot y_M + cos\alpha \cdot K_m^x \cdot sin\alpha \cdot y_M + cos^2\alpha \cdot K_m^y \cdot x_M)sin\psi + (-cos\alpha \cdot K_m^y \cdot sin\alpha \cdot x_M - sin\alpha \cdot K_m^x \cdot cos\alpha \cdot x_M - sin^2\alpha \cdot K_m^x \cdot y_M + cos^2\alpha \cdot K_m^y \cdot y_M)cos\psi + (-sin\alpha^2 \cdot K_m^x + cos\alpha^2 \cdot K_m^y)y + (-cos\alpha \cdot K_m^y \cdot sin\alpha - sin\alpha \cdot K_m^x \cdot cos\alpha)x + cos\alpha \cdot K_m^y \cdot sin\alpha \cdot x_M - cos^2\alpha \cdot K_m^y \cdot y_M + sin\alpha \cdot K_m^x \cdot cos\alpha \cdot x_M + sin^2\alpha \cdot K_m^x \cdot y_M$$

with:

$$S_{/_{R_0}} = M_{/_{R_p}} = \begin{bmatrix} x_M \\ y_M \end{bmatrix}$$

3.4. *Final magnetic configuration of the platform*

Figure 9 represents the final magnetic configuration of the platform. This configuration has been chosen to simplify the non linear expression of the magnetic force $\boldsymbol{F}^{mag}$ (given by (12)) and to limitate the coupling between the various directions of measurement. These simplifications will be exploited in the linear modeling of the platform dynamic. This configuration is based on 2 pairs of fixed cubic magnets p_1 and p_2 (5×5 mm) and 2 cylindrical moving magnets M_1 and M_2 placed at two corners of the platform, inside a float. Two empty floats are placed at the third and fourth corners in order to ensure the stability of the square platform along $\boldsymbol{z}$ axis. The center of gravity G is the center of $[M_1M_2]$. The positions of S_i and M_i are :

$$S_{1/_{R_0}} = M_{1/_{R_p}} = \begin{bmatrix} \delta \\ 0 \end{bmatrix} \qquad S_{2/_{R_0}} = M_{2/_{R_p}} = \begin{bmatrix} -\delta \\ 0 \end{bmatrix}$$

3.5. *Linear dynamic model of the optimized platform*

The floating platform is considered as a rigid body of mass m with a center of gravity G and having a moment of inertia tensor J. The linear dynamic model is going to be established from the differential equations given by the platform dynamic behavior in the plan (xOy):

$$\boldsymbol{F}_{p_1}^{mag} + \boldsymbol{F}_{p_2}^{mag} + \boldsymbol{F}^{v}_{/_{R_0}} + \boldsymbol{F}^{ext}_{/_{R_0}} = m\ddot{\boldsymbol{G}}_{/_{R_0}} \tag{13}$$

The perturbation forces are neglected. $\boldsymbol{F}_{p_1}^{mag}$ is the magnetic force applied by p_1 on M_1, $\boldsymbol{F}_{p_1}^{mag}$ is the magnetic force applied by p_2 on M_2, $\boldsymbol{F}^{v}$ is the viscous friction force between the float and water and $\boldsymbol{F}^{ext}$ is the external force applied on the platform. In case of small displacements:

$$\boldsymbol{F}^{v} = K_v \cdot \dot{\boldsymbol{G}} = \begin{bmatrix} K_v^x & 0 \\ 0 & K_v^y \end{bmatrix} \cdot \dot{\boldsymbol{G}} \tag{14}$$

Equation (13) projected onto the $\boldsymbol{x}$ and the $\boldsymbol{y}$ axis gives:

$$\begin{cases} m\ddot{X} = -2K_m^x \cdot X - K_v^x \cdot \dot{X} + F_x^{ext} \\ m\ddot{Y} = -2K_m^y \cdot Y - K_v^y \cdot \dot{Y} + F_y^{ext} \end{cases} \tag{15}$$

The dynamic behavior in case of circular movement is given by:

$$\sum \mathcal{M}/_G = J\dot{\Omega}$$
$$\Rightarrow \boldsymbol{F}_{p_1}^{mag} \wedge \boldsymbol{GM_1} + \boldsymbol{F}_{p_2}^{mag} \wedge \boldsymbol{GM_2} + \zeta_v + \zeta^{ext} = J\dot{\Omega} \tag{16}$$

with Ω the instantaneous rotation vector.

The projection of equation (16) onto the $\boldsymbol{z}$ axis, gives:

$$J_\psi\ddot{\psi} = 2((K_m^x - K_m^y)cos\psi - K_m^x) \cdot sin\psi \cdot \delta^2 - K_v^{rot}\dot{\psi} + \zeta^{ext}$$

For very small ψ $sin\psi \approx \psi$ and $cos\psi \approx 1$, thus:

$$J_\psi\ddot{\psi} = -2K_m^y\psi\delta^2 - K_v^{rot}\dot{\psi} + \zeta^{ext} \tag{17}$$

3.6. *Measurement of the platform position*

The determination of X, Y and ψ is done with three displacement sensors [1] mounted in an optimized configuration shown in figure 10 (only the third sensor is completely drawn). These three sensors measure respectively three distances l_1, l_2 and l_3. To calculate X, Y and ψ each sensor measurement is modelized:

$$\begin{cases} P_i : \text{origin of measurement} \\ \boldsymbol{d}_i : \text{light beam direction} \\ I_i : \text{light beam target on the deflector } D_i \\ \boldsymbol{n}_i : \text{normal to the deflector surface} \end{cases} \tag{18}$$

In this configuration, $\boldsymbol{d}_i$ and $\boldsymbol{n}_i$ are collinear when the platform is on its equilibrium position. The distances l_1, l_2 and l_3 measured by the sensors are given by:

$$\begin{cases} l_1 = \|\boldsymbol{P_1 I_1}\| = -X\,\tan\psi + Y + \delta\,\tan\psi \\ l_2 = \|\boldsymbol{P_2 I_2}\| = -X\,\tan\psi + Y - \delta\,\tan\psi \\ l_3 = \|\boldsymbol{P_3 I_3}\| = X + Y\,\tan\psi - \delta\,\tan\psi \end{cases} \tag{19}$$

with:

$$P_1 = \begin{bmatrix} \delta \\ 0 \end{bmatrix}_{/R_0},\ P_2 = \begin{bmatrix} -\delta \\ 0 \end{bmatrix}_{/R_0} \text{ and } P_3 = \begin{bmatrix} 0 \\ \delta \end{bmatrix}_{/R_0}$$

Inversion of the non linear equations (19) gives:

$$\tan\psi = \frac{l_1 - l_2}{2\delta} \tag{20}$$

$$X = \frac{\delta\left(2\,\delta\,l_1 - 2\,\delta\,l_2 + 4\,\delta\,l_3 - {l_1}^2 + {l_2}^2\right)}{4\,\delta^2 + {l_1}^2 - 2\,l_1\,l_2 + {l_2}^2} \tag{21}$$

$$Y = \frac{\delta\left({l_1}^2 - 2\,l_1\,l_2 + 2\,l_1\,l_3 + {l_2}^2 - 2\,l_2\,l_3 + 2\,\delta\,l_1 + 2\,\delta\,l_2\right)}{4\,\delta^2 + {l_1}^2 - 2\,l_1\,l_2 + {l_2}^2} \tag{22}$$

4. Models comparison

This section is devoted to some comparisons between the linear model (15)(17) versus the physical model (13)(16) taken as a reference. In the non linear model, magnetic and electromagnetic forces are computed at each simulation time step with a complete analytical calculation of magnetic fields in M_1 and M_2. Influences of *all* magnets p_i are taken into account. The coupling between the different measurement directions is also taken into account in the mechanical equations (13)(16) which are numerically solved with a representation using quaternions.

[1] Using confocal chromatic principle and designed by STIL SA

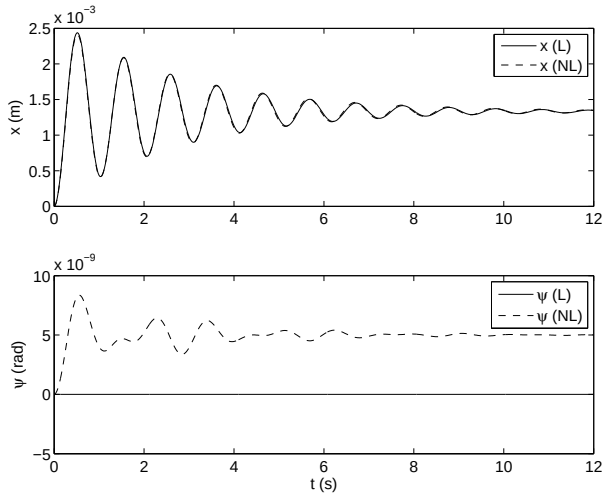

Fig. 11. Responses along $\boldsymbol{x}$ and ψ of linear (L) and non-linear (NL) models for a step force $F_x^{ext} = 68\ \mu N$

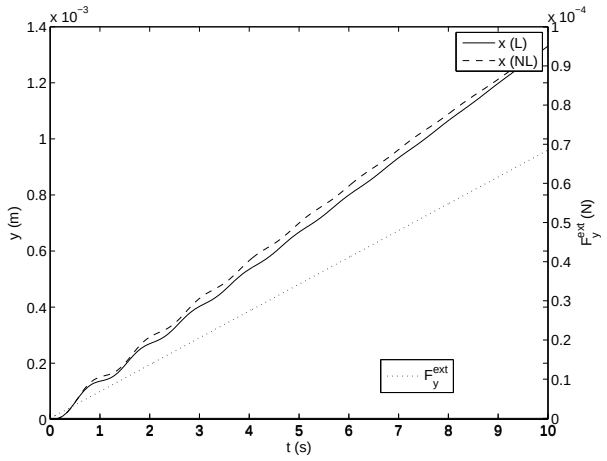

Fig. 12. Responses along $\boldsymbol{y}$ of linear (L) and non-linear (NL) models for a ramp force F_y^{ext}

Figure 11 shows the step responses in R_0 along $\boldsymbol{x}$ and ψ for a step force $F_x^{ext} = 68\ \mu N$. The differences between linear and non-linear models responses are very small in this case. The response will be the same along $\boldsymbol{y}$ for a step force applied to the platform along $\boldsymbol{y}$. The very small non-linear response $\psi(t)$ (less than 10^{-8} rad) is different from zero only because of numerical computational errors. Figure 12 shows the two models responses along $\boldsymbol{y}$, for a force ramp F_y^{ext}. A small difference between the two models responses in the transient response can be noted. Figure 13 shows the step responses along $\boldsymbol{x}$ and ψ, for a big step force F_x^{ext} equal to $0.3\,mN$. The large differences are due to the non linearity of the magnetic force $\boldsymbol{F}^{mag}$ in case of large displacements far from the stable equilibrium points S_i. The differences on ψ are still due to numerical computational errors.

5. Experimental setup

The experimental setup is schematized on the figure 14. The corresponding picture is on the figure 15. It has two

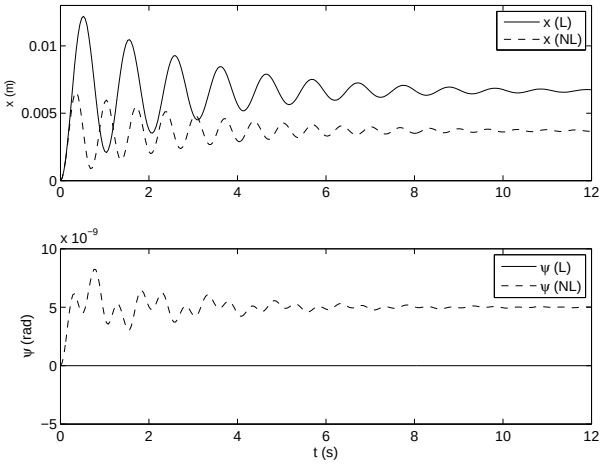

Fig. 13. Responses along $\boldsymbol{x}$ and $\boldsymbol{\psi}$ of linear (L) and physical (NL) models for a step force $F_x^{ext} = 0.3\ mN$

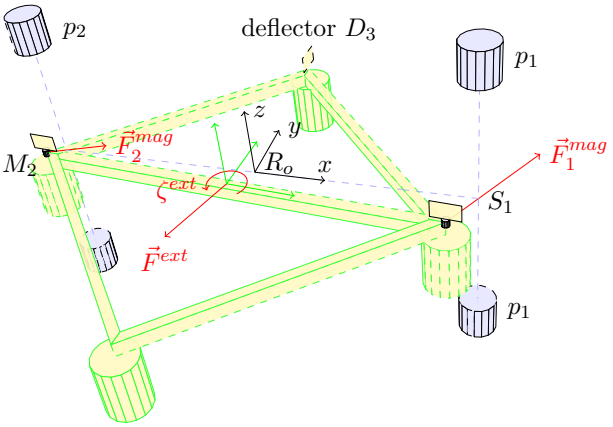

Fig. 14. Diagram of the experimental setup

pairs of fixed magnet p_1 (tag ①) and p_2 (tag ②). The two magnets M_1, M_2 are stuck on the platform (tag ③ for M_2) which has four floats and three deflectors D_1, D_2, D_3 (tag ④ for D_3). A tank is filled of water and placed under the platform (tag ⑤). The sensitive area is localized in the center of the platform (tag ⑥). The three confocal sensors (tag ⑦) are disposed in front of each deflector and measure the distances l_1, l_2, l_3. Additional coils are fixed on the setup (tag ⑧). They are used during the calibration process (see section 6). When supplied with a current, these coils modify the local magnetic field around the floating magnets M_1 and M_2. This produces an electromagnetic excitation force that move the platform along $\boldsymbol{x}$, $\boldsymbol{y}$ and around $\boldsymbol{z}$.

The sensor is designed to measure three components of both external force and torque which are applied on the sensitive area: F_x^{ext} and F_y^{ext} in the plan (xOy) and torque ζ^{ext} around $\boldsymbol{z}$. With this configuration, the corresponding displacement X, Y, ψ is deducted from the measurements given by the three confocal sensors with equations (20-22). In steady state, the estimation $\hat{F}^{ext}$ of the applied force and torque is calculated by :

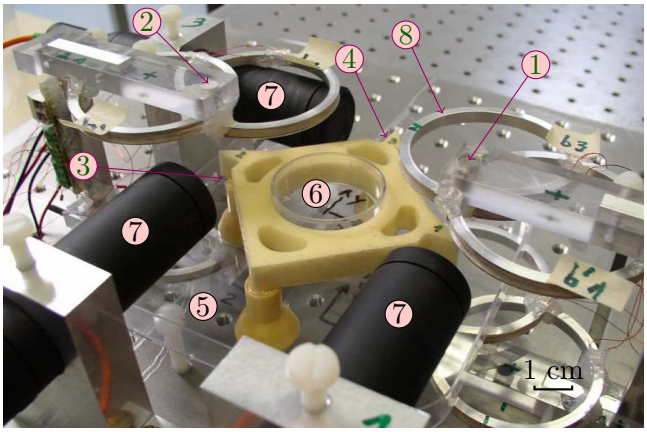

Fig. 15. Experimental setup of the force sensor.

$$\hat{F}^{ext} = K_m \cdot \boldsymbol{d} \quad \Leftrightarrow \quad \begin{vmatrix} \hat{F}_x^{ext} \\ \hat{F}_y^{ext} \\ \hat{\zeta}^{ext} \end{vmatrix} = K_m \begin{vmatrix} X \\ Y \\ \psi \end{vmatrix}. \qquad (23)$$

K_m is the platform magnetic stiffness matrix that has to be identified. For small displacements of the platform, K_m is independent of $\boldsymbol{d}$.

K_m can be easily deduced from equations (15) and (17) in steady state:

$$K_m = \begin{bmatrix} 2K_m^x & 0 & 0 \\ 0 & 2K_m^y & 0 \\ 0 & 0 & 2\delta^2 \cdot K_m^y \end{bmatrix}$$

6. State model identification and sensor calibration

Generally, calibration is a complex problem for micro and nano force sensors because of the lack of standard forces at this scale [13]: no international measurement institute supports a direct force realization linked to the International System of Units (SI) below 1 N, even for static force. Thus, calibration must be performed using indirect static or dynamic approaches and care must be taken with stiffness calculation. Several dynamic calibration methods have been investigated for force sensors using levitating mass. These methods are based on particular external force generation like impact force [14], step force [15] and oscillating force [16]. The chosen calibration approach is based on a zero input force response (ZIR) and only requires a pulse current in the magnetic coils to briefly change the magnetic field and to set the platform into free damped oscillations with unknown initial conditions. Because the platform linear model is decoupled, it is possible to generate successive excitations along the three measurement directions $\boldsymbol{x}$, $\boldsymbol{y}$ and ψ and to measure the corresponding platform ZIR.

The platform model is identified with the experimental prototype shown in the figure 15 (m=0.004 kg). The lin-

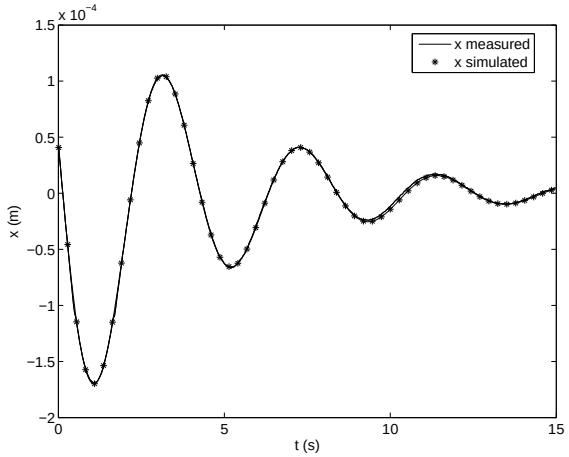

Fig. 16. Measured and identified zero input response of the platform along $\boldsymbol{x}$

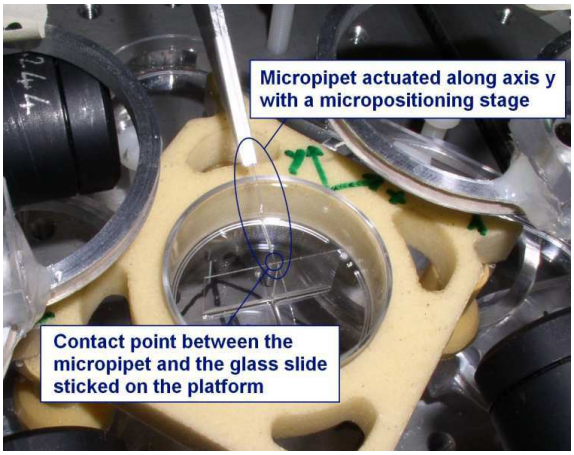

Fig. 17. Application of a F_y^{ext} force with a microcapillary effector.

ear model of the platform requires to identify the stiffness and the damping of the mass. This identification process is performed using Matlab identification Toolbox (state-space model identification from ZIR with unknown initial conditions).

Figure 16 shows the matching (97%) between the non linear measured zero input response along $\boldsymbol{x}$ and the identified linear one. Identifications along y and ψ give similar results. The obtained values are :

$$K_m^x = 11.82 \times 10^{-3} \text{ N/m}, \quad K_v^x = K_v^y = 1.83 \times 10^{-3} \text{ N.s/m}$$
$$K_m^y = 9.46 \times 10^{-3} \text{ N/m}, \quad K_v^{rot} = 4.43 \times 10^{-7} \text{ N.s/rad}$$

Thus, the identified platform magnetic stiffness matrix is:

$$K_m = \begin{bmatrix} 0.0236 & 0 & 0 \\ 0 & 0.0189 & 0 \\ 0 & 0 & 0.000017 \end{bmatrix}$$

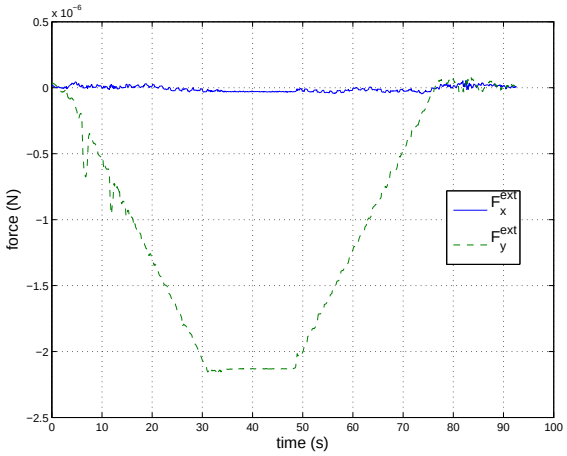

Fig. 18. Sensor response to a real F_y^{ext} force.

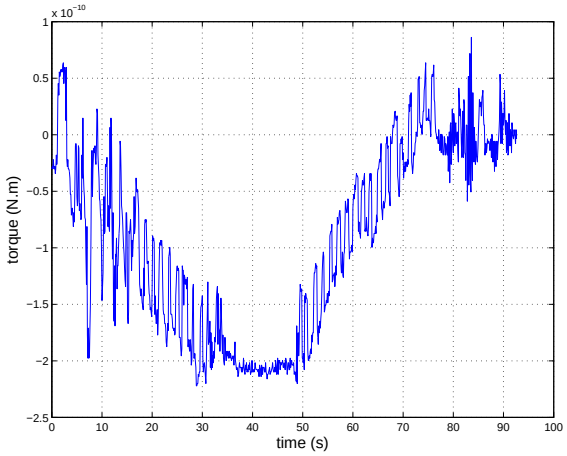

Fig. 19. Sensor response to a real F_y^{ext} force.

7. Experimental force and torque measurement

In this section, the passive measurements principle (23) is illustrated in quasi steady-state. In this case, the dynamic of the platform is neglected. On the experimental setup a micro-positioning stage (PI M122) has been added in order to move a glass micro-pipet along the y direction. This effector is used to apply a force F_y^{ext} on the platform. The tip (20 μm in diameter) of the pipet moves to a contact point localized near the center of the platform as shown in figure 17. The contact area on the platform is a stuck glass slide (0.3 mm of thickness) that is parallel to the xOz plane. The contact point has been chosen as near as possible of the center of gravity G of the platform. The figure 18 shows the response of the sensor to this solicitation. The effector initially placed a few micrometers from the slide is moved against it at a speed of 5 μm/s until the measured force F_y^{ext} reach the value of -2.5 μN. After 15 seconds the effector is moved back until the contact between the effector and the slide is broken (no pull-off force is measured in this experiment). During the test the component F_x^{ext} remains at zero. The measured torque is smaller than 2^{-10} N.m (see figure 19). On the torque curve

the shape of F_y^{ext} is visible. This phenomenon is due to the fact that the contact point is not strictly superposed with G, thus a torque is measured.

After the unloading (contact loss), the displacement of the platform always comes back to zero. If a static hysteresis on the displacement was present, this couldn't be the case. The influence of the meniscus evolution between the water and the floats has not be identified. Meniscus evolution should generate transient forces and necessarily transient rotation and translation of the platform. This question is open. The resolution in force or torque estimation depends on the measurement noise of the confocal sensors but also (and mostly) on the environmental seismic and acoustic vibrations that generate unwanted displacements of the platform (see figure 1). The environment where the experiments are realized is not specially favorable to reach a low level of noise: the sensor is located on a first floor that is poorly decoupled from the building vibrations. There is also heavy building work (building extension under construction). Measurements done during the night are more representative of the resolution that can be reached. In these conditions the typical standard deviation obtained is $\sigma_F = 3 \times 10^{-9}$ N for the force and $\sigma_\psi = 2.7 \times 10^{-12}$ N.m for the torque.

8. Potential applications

This sensor can be used to characterize the mechanical stiffness of micro-objects like for instance AFM cantilevers. Like in the previous section, a vertical edge need to be stuck on the platform near the centre of gravity G. The tip of the cantilever is moved along x axis in R_0 with a micro-positionning stage (see figure 20) until the contact is established between the tip and the edge. The tip is then pushed against the edge in the x direction and thus apply an external force with a component F_x^{ext} in R_0. If the contact point is different from G, a torque ζ^{ext} around z will be also measured. These components are measured by the force sensor. In the same time, the bending δx of the tip along axis x is measured with a specific displacement sensor L placed on the positionning stage. The stiffness K_{object}^x of the cantilever is then:

$$K_{object}^x = \frac{\hat{F}_x^{ext}}{\delta x} \tag{24}$$

Another potential application that needs to be investigated is to use this sensor as a a nanotribometer in order to characterize the mechanical friction properties of a multi-asperity contact between two objects. Like previously, the first object with a planar vertical edge (normal to x axis in R_0) is stuck on the platform near G. The second object (here spherical) is placed on a micro-positionning stage and moving along x axis in R_0 until the contact is established between the two objects (see figure 21). The second object is then pushed against the edge in the x direction and thus

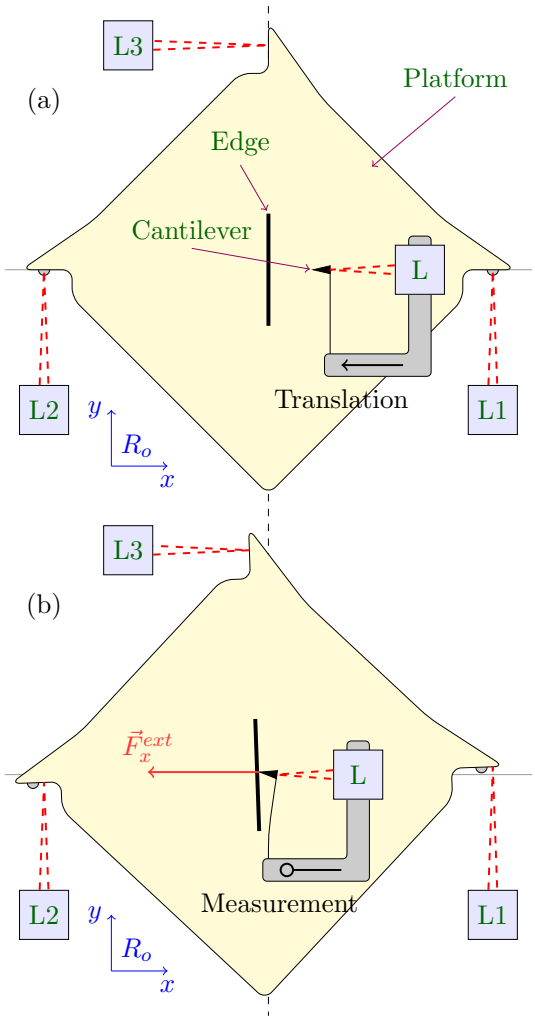

Fig. 20. Application of the sensor to stiffness caracterization.

apply to it a force with component F_x^{ext} that is measured by the force sensor. The contact point must be adjusted to have $\zeta^{ext} \cong 0$. The displacement in the $\boldsymbol{x}$ direction is stopped in order to set the normal force F_x^{ext} to a given reference value (loading force that should not change). The micro-positionning stage is then moved forward and backward along the y direction in R_0 and the tangential friction force F_y^{ext} between the two objects is measured by the force sensor. Normally the measured torque $\hat{\zeta}^{ext}$ around z must remain close to zero to have a valid friction force measurement. Obviously the last condition will be difficult to hold with a passive force sensor. An active version of the sensor that enable to control with coils the position and orientation of the platform while measuring the external force is currently under development and should be more appropriate for this.

9. Conclusion

A dynamic modeling and identification of a micro and nano force sensor designed to measure planar force and vertical torque has been presented. This sensor is based on

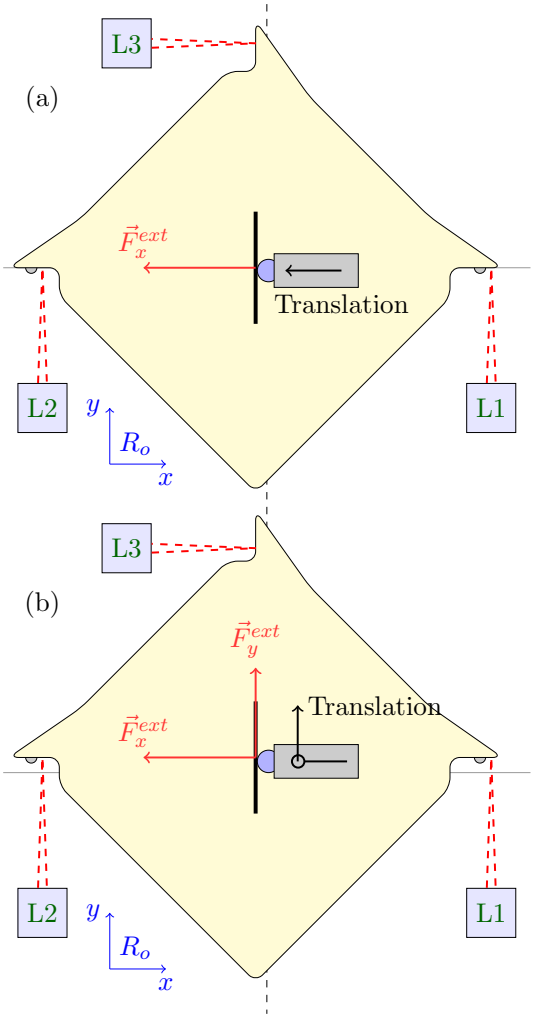

Fig. 21. Application of the sensor to tribology.

a seismic mass sensitive to external forces. This mass is a floating platform naturally stable in the space thanks to passive magnetic springs and upthrust buoyancy. The mechanical stiffness of the developed experimental prototype is about 0.0236 N.m^{-1} along $\boldsymbol{x}$ and 0.0189 N.m^{-1} along $\boldsymbol{y}$. Two models describing the platform dynamic have been developed. First, a physical model used as a reference model and secondly, a simplified linear model whose performances have been compared to the non-linear model. The linear model identification shows that the dynamic behavior of the prototype sensor is closed to the behavior expected. The absence of dry friction in the measurement directions associated with a low stiffness makes the sensor highly sensitive (resolution equal to a dozen of nanonewton). In the other spatial directions or orientations, micro forces or torques measurement is not possible because of the high stiffness caused by the upthrust buoyancy. Nevertheless, the model developed in this article doesn't take into account the effect of reflected delayed liquid wave generated by the platform displacements. The future work will consist in improving the capabilities of the sensor by choosing a deconvolution law which will take into account the dynamic of the platform, in order to estimate correctly slowly varying force and torque.

Acknowledgment

The material presented here was based upon works supported by the French National Research Agency (three years project STILμForce ANR-07-ROBO-0005).

References

[1] M. Sepaniak, P. Datskos, N. Lavrik, and C. Tipple, "Microcantilever transducers: A new approach in sensor technology," *Analytical chemistry*, pp. 568–575, 2002.

[2] P. Rougeot, S. Régnier, and N. Chaillet, "Forces analysis for micro-manipulation," in *Proceedings 2005 IEEE international symposium on computational intelligence in robotics and automation*, 2005, pp. 105–110.

[3] N. Kato, I. Suzuki, H. Kikuta, and K. Iwata, "Force-balancing microforce sensor with an optical-fiber interferometer," *Review of scientific instruments*, vol. 68, pp. 2475–2478, 1997.

[4] F. Arai, A. Kawaji, T. Sugiyama, Y. Onomura, M. Ogawa, T. Fukuda, H. Iwata, and K. Itoigawa, "3d micromanipulation system under microscope," in *International symposium on micromechatronics and human science*, 1998, pp. 127–134.

[5] Y. Sun, W. Kai-Tak, K. Roberts, J. Bischof, and J. Bradley, "Mechanical property characterization of mouse zona pellucida," *IEEE transactions on nanobioscience*, vol. 2, no. 4, pp. 279–285, 2003.

[6] W. Li and N. Xi, "Novel micro gripping, probing and sensing devices for single-cell surgery," in *Proceedings of the 26th international conference of the IEEE EMBS*, 2004, pp. 2591–2594.

[7] Y. Shengyuan and S. Taher, "Micromachined force sensors for study of cell mechanics," *Review of scientific instruments*, vol. 76, no. 4, 2005.

[8] M. Boukallel, E. Piat, and J. Abadie, "Passive diamagnetic levitation: theoretical foundations and application to the design of a micro-nano force sensor," in *Proceedings of the 2003 IEEE/RSJ intl. Conference on Intelligent Robots and Systems Las Vegas, Nevada*, 2003, pp. 1062–1067.

[9] M. Boukallel, J. Abadie, and E. Piat, "Levitated micro-nano force sensor using diamagnetic levitation," in *Proc. of the IEEE International Conference of Robotics and Automation*, 2003, pp. 3219–3224.

[10] F. Bancel and G. Lemarquant, "Three-dimensional analytical optimization of permanent magnets alternated structure," *IEEE Transactions on Magnetics*, vol. 34, no. 1, pp. 242–247, 1998.

[11] S. Earnshaw, "On the nature of the molecular forces," *trans. Cambridge phil.Soc.*, pp. 97–112, 1842.

[12] A. Boerdijik, "Technical aspects of levitation," *Philips research reports*, pp. 45–46, 1956.

[13] Y. Fujii, "Methode for generating and measuring the micro-newton level forces," *Mechanical Systems and Signal Processing*, vol. 20, pp. 1362–1371, 2006.

[14] Y. Fujii and H. Fujimoto, "Proposal for an impulse response evaluation method for force transducers," *Measurement Science and Technology*, vol. 10, no. 4, pp. N31–N33, 1999.

[15] Y. Fujii, "Proposal for a step response evaluation method for force transducers," *Measurement Science and Technology*, vol. 14, no. 10, pp. 1741–1746, 2003.

[16] R. Kumme, "Investigation of the comparison methode for the dynamic calibration of force transducers," *Measurement*, vol. 23, no. 4, pp. 239–245, 1998.

List of Figures